

RESEARCH ARTICLE

Online Real-Time SOH Prediction and Anomaly Detection Under Dynamic Load Conditions and Nonstandard Practice

SUKHAN LEE¹, (Life Fellow, IEEE), AND AREUM KIM

School of Artificial Intelligence, Sungkyunkwan University, Suwon, Gyeonggi-do 16429, Republic of Korea

Corresponding author: Sukhan Lee (Lsh1@skku.edu)

This work was supported in part by the Korea Health Technology Research and Development Project through Korea Health Industry Development Institute (KHIDI), sponsored by Ministry of Health and Welfare (MOHW), South Korea, under Grant HW20C2077; in part by the e-Drive Train Platform Development Project of Korean Energy Technology Evaluation and Planning (KETEP), sponsored by Ministry of Tread, Industry and Energy (MOTIE), under Grant KETEP 20172010000420; in part by the Artificial Intelligence (AI) Graduate School Program under Grant 2019-0-00421; and in part by the Information and Communication Technology (ICT) Consilience Program, Institute of Information and Communications Technology Planning and Evaluation (IITP), sponsored by Ministry of Science and ICT (MSIT), South Korea, under Grant IITP-2020-0-01821.

ABSTRACT For effective battery management, accurate prediction of battery state-of-health (SOH) and timely detection of anomalies is required. Despite recent advances, real-world battery management has yet to overcome such difficult issues as life-cycle SOH prediction and anomaly detection for early warning and fault tracing under realistic operational conditions. In this study, we present an approach for online real-time SOH prediction and anomaly detection for rechargeable batteries throughout their life cycles with a focus on real-world applicability. First, we present a model-based prediction of battery states under normal aging, which serves as a reference for detecting an anomaly. To that end, we propose a method for updating model parameters and their uncertainties cyclically and temporally based on the predicted SOH. In particular, we develop a method for SOH prediction under realistic conditions such as inter- and intracycle variations in load current as well as nonstandard charging and discharging practices. Finally, by fusing the model-predicted state with the measured terminal voltage and current, we achieve a statistically well-defined decision on an anomaly. Experiments using CALCE and custom-collected datasets validate the effectiveness of the proposed method in terms of accuracy and sensitivity for detecting abrupt and slow modes of anomaly.

INDEX TERMS Anomaly detection, covariance projection filter, equivalent circuit model, rechargeable battery, state of health.

I. INTRODUCTION

Rechargeable batteries play an important role in smart cities and transportation as energy storage and distribution solutions. This creates an ever-increasing demand for an effective and efficient method of battery management, particularly, to ensure safety. In addition, for battery management, online real-time SOH prediction and anomaly detection represent a key enabler for warning, tracing, and diagnosing faults, as well as avoiding potentially hazardous situations such as abnormal charge depletion, thermal runaway, and fire. Other than manufacturing defects and sensor failures, battery anomalies can occur due to over-charging, over-discharging,

battery imbalance, overheating, external or internal short-circuit, and electrolyte leaks [1]. For real-world applicability, online real-time anomaly detection should be performed during any of their charging and discharging cycles while the batteries are in use. Furthermore, it is preferable for anomaly detection to deal with both abrupt and slow modes of anomalies so that the anomalies can be traced and maintained with early warning. For an online real-time setting, anomaly detection is preferred to being based on such quantities as terminal voltages and currents that are readily measurable under actual battery operations. Measuring anomaly indicators such as internal resistance, Coulomb count, diffusivity, and electrochemical impedance spectrum (EIS) using an offline arrangement or a specialized apparatus [2] is considered impractical.

The associate editor coordinating the review of this manuscript and approving it for publication was Ganesh Naik¹.

Battery anomaly detection has advanced toward a more reliable and informative anomaly decision for effective battery management. The many approaches developed to date for anomaly detection can generally be grouped into 1) the identification of abnormal behavior of batteries as an outlier from the cluster representing the distribution of normal behaviors of batteries or a pack of family cells [3], [4], [5], [6], [7], [8], [9], [10] and 2) the deviation of the observed behavior of a battery from the reference behavior predicted as normal [11], [12], [13], [20], [21], [22], [23], [24]. Various data-driven and model-based approaches have been proposed as the methodologies for implementing the two groups of anomaly detection described above, as introduced in the following.

Data-driven approaches to identifying an abnormal cell in a battery pack have been developed based on thresholding the distance between the representative state of the pack and the observed state of the cell. To ensure robustness in anomaly decisions, there have been explored more reliable distance metrics [3], such as the median absolute deviation (MAD) [4], as well as more comprehensive threshold settings [5]. Bhaskar et al. [3] proposed the evaluation of mean-based residuals of cells by the principal component analysis (PCA) for the detection of an abnormal cell in a pack as an outlier. They also found the importance of including temperature as battery state, besides terminal voltage, in anomaly detection. Liu et al. [6] proposed a convolutional neural network (CNN) classification of faulty cells in a battery pack as those cells having their discharge voltage curves different from the majority of cells in the pack. Yao et al. [7] proposed a general regression neural network with the voltage difference and covariance between cells as input features to diagnose a fault. Haider et al. [8] proposed the K shape-based hierarchical clustering of time series data with the cross-correlation distance metrics to identify a faulty battery from a pack when the battery changes its initial membership and ranks among the charge-cycle mean voltage clusters. Due to the difficulty of collecting anomaly data from various fault sources as well as over a battery life cycle, most data-driven approaches resort to the data representing the distribution of normal behaviors while anomalies are detected based on the statistical inconsistency existing in the behavior of a battery under examination. To this end, autoencoder (AE) and variational autoencoder (VAE) frameworks are commonly adopted to encode the distribution of normal behaviors in their latent space by learning. Sun et al. [9] proposed a VAE framework with a gated recurrent unit (GRU) to learn the multivariate time series data of a battery pack and detected potential anomalies of a cell based on a large reconstruction error for the input data from the cell. Data-driven approaches can also be applied to identifying the deviation of the observed behavior of a battery from the reference behavior predicted as normal. Shin et al. [10] proposed to learn the correlation existing between terminal voltage and current by using a sequence-to-sequence deep learning model with the training data representing battery normal behaviors.

Anomalies are detected by comparing the measured voltage with the reference voltage predicted by the learned model with the measured current as input.

On the other hand, model-based approaches detect anomalies in the process of filtering the predicted battery normal states from the model with the measured terminal states. Gadsden and Habibi [11] used a smooth variable structure filter to detect resistor and capacitor faults by calculating how close the filtered model is to the true model in an interacting multiple-model framework. Liu and He [12] proposed a method for detecting sensor faults based on the residual between estimated and measured output voltages, where the output voltage is estimated using a state observer applied to the second-order RC network model. Tunga et al. [13] proposed a windowed Chi-square detector for sensor fault detection based on a moving sum of residuals over a sliding window, making the approach more adaptive than a static detector with a one-shot observation. For model-based approaches, the quality of the model used to predict the battery states under normal aging is key for robust anomaly detection. There are three basic approaches to modeling batteries. They are the physics-based model [14], [15], the equivalent circuit (EC) model [16], [17], and the empirical state-space model [18]. Refer to [19] for the details of battery models available to date and the comparative analysis of their strengths and weaknesses. For anomaly detection, a model should be precise enough for representing the actual operational dynamics of a battery, yet uncomplicated and general enough for real-time battery management with cell sampling. In particular, a model should accurately represent the life-cycle aging behavior of batteries, which is considered normal, under a wide variation of operational conditions. There have been proposed approaches to the real-time fitting of model parameters to actual measurements for the online real-time update of a model so as to follow battery aging while handling discrepancies among individual batteries [20], [21], [22], [23], [24]. However, the real-time fitting of a model to measurements may result in an undesirable side-effect for anomaly detection by allowing the model to adapt to abnormal behaviors.

Data-driven approaches rely on their performance largely on the quality of collected training data, as statistically biased and misrepresented data results in erroneous decisions. Whereas model-based approaches rely their performance on the quality of the model used to predict the battery states under normal aging. However, collecting a sufficient size of statistically well-represented training data as well as modeling the true aging behavior of batteries under complex nonlinear electrochemical battery dynamics [25] have remained a real challenge. The challenge becomes especially keen, should we take into account wide variations in operational conditions, including variations in dynamic load conditions, charging and discharging practices, operational temperatures, etc., over long battery life cycles.

In this study, we propose an approach to online real-time anomaly detection for rechargeable batteries in consideration

of such realistic operational conditions as variations in dynamic load conditions, non-standard charging and discharging practices, as well as variations in operational temperatures. Furthermore, the proposed approach also allows anomaly detection to be executed any at time during the battery life cycles. The proposed approach is based on the cyclic iteration of the following processes, 1) the data-driven deep prediction of battery SOH under normal aging, 2) the temporal update of model parameters based on the predicted SOH, 3) the model-based real-time prediction of battery normal states, and 4) the decision on an anomaly in the process of fusing the predicted state and measured terminal voltage. The novel contributions of this study are summarized as follows: 1) A hybrid approach to any-cycle and any-time prediction of normal battery states under aging is established for use in anomaly decisions. To this end, a method for cyclically and temporally updating model parameters and their uncertainties based on the predicted SOH as well as operational temperature is presented. 2) Furthermore, the proposed SOH prediction fully accounts for such realistic operational conditions as dynamic load current variations and nonstandard practices in charging and discharging. To this end, the minimum charging and discharging voltage ranges required for sufficient accuracy in SOH prediction under nonstandard practices are established for the first time. 3) To alleviate a possible combinatorial explosion in standard and non-standard mixtures in LSTM-based SOH prediction, a novel method for transforming the LSTM input indices from nonstandard practices equivalently to those corresponding to standard practices is proposed. 4) The covariance projection filter (CPF) [26], [27] is introduced not only to obtain statistically well-defined anomaly decisions but also to provide a probabilistic distance metric to indicate the deviation from normalcy, especially, for monitoring a slow mode of anomalies.

This paper is organized as follows: Section II introduces the battery EC model used for representing a battery aging behavior and the CPF used for probabilistic decisions on the anomaly. Section III discusses the overall flow of the proposed anomaly detection process. Section IV introduces a stacked LSTM and its four input indices used for SOH prediction under realistic conditions. Section V presents the SOH-based estimation of time-varying battery model parameters. Section VI describes the CPF-based fusion of the model-predicted state and the measured terminal voltage for anomaly decisions. Finally, Section VII presents the experimental validation of the proposed method based on the CALCE [28] and custom-collected datasets.

II. BACKGROUND

A. MODELING BATTERY STATE EQUATION UNDER NORMAL AGING

Fig. 1 depicts the first-order RC network EC model of a lithium-ion battery with cyclically and temporally varying model parameters to represent a battery's normal aging

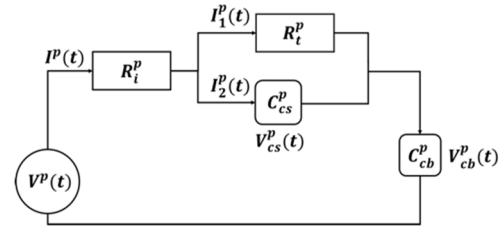


FIGURE 1. The first-order RC network model of a lithium-ion battery, where p and t denote, respectively, the p^{th} cycle and the time lapse from the start of discharging.

behavior. From Fig. 1, the battery state equation at the p^{th} cycle can be expressed as follows:

$$\begin{bmatrix} dSOC^p(t)/dt \\ dV_{cs}^p(t)/dt \end{bmatrix} = \begin{bmatrix} I^p(t)/k^p(t)C_{cb}^p \\ -V_{cs}^p(t)/R_t^pC_{cs}^p + I^p(t)/C_{cs}^p \end{bmatrix} + \begin{bmatrix} w_1^p(t) \\ w_2^p(t) \end{bmatrix} \quad (1)$$

$$v^p(t) = k^p(t)SOC^p(t) + V_{cs}^p(t) + I^p(t)R_t^p + d^p(t) + [w_3^p(t)] \quad (2)$$

where $v^p(t)$, $I^p(t)$ are the respective terminal voltage and current at the time t , R_t^p the internal resistance at the p^{th} cycle, and $w_i^p(t)$, $i = 1, \dots, 3$, the uncertainties involved.

$SOC^p(t)$ indicates the battery state of charge (SOC) at the p^{th} cycle, defined as the percentage of releasable charge capacity relative to the battery-rated charge capacity. The battery open circuit voltage (OCV) at the p^{th} cycle, $OCV^p(t)$, can be obtained from Eq. (2) with $I^p(t) = 0$, $OCV^p(t) = k^p(t)SOC^p(t) + d^p(t)$. In Section V, we show that $k^p(t)$ and $d^p(t)$ can be estimated from the p^{th} cycle SOC-OCV curve derived from SOH^p , while R_t^p is cyclically updated by the functional relationship of R_t^p with SOH^p . The remaining model parameters, the polarization resistance, R_t^p , the surface capacitance, C_{cs}^p , and the bulk capacitance, C_{cb}^p , are subjected to cyclic degradation the rate of which is affected by battery operational temperature. Table 1 shows the variation of degradation rates and their uncertainty bounds for R_t , C_{cs} , and C_{cb} along cycles. They are created by computing the average degradation rates and their maximum deviation over the typical temperature range between 25°C and 55°C, which is based on the experimental data on degradation rates with respect to cycles and operational temperatures [28].

TABLE 1. Average degradation rate and their uncertainty bound due to operational temperature variation.

Cycle No.	Average Degradation Rate ± Max. Uncertainty Bound (%) along Cyclic Progression				
	50	100	150	200	250
SOH	1.36 ±0.54	2.87 ±1.21	4.12 ±1.76	6.51 ±1.80	8.19 ±2.26
R_t	11.54 ±10.86	22.21 ±16.98	36.98 ±27.11	47.40 ±27.44	58.08 ±29.45
C_{cs}, C_{cb}	0.57 ±0.38	0.91 ±0.57	1.36 ±0.87	1.82 ±1.13	2.21 ±1.37

For accurate detection of anomalies based on (1) and (2), it is necessary that the uncertainties associated with the state and measurement, $w_i(t)$, $i = 1, \dots, 3$, should be well-defined at time t . When defining uncertainties, we consider variations within the typical range of operational temperature, as well as errors in state prediction and measurement. Specifically, first, the uncertainty bounds of $k^p(t)$, $d^p(t)$ and R_i^p , $\Delta k^p(t)$, $\Delta d^p(t)$ and ΔR_i^p , respectively, are achieved from the uncertainty bound of the predicted SOH^p , ΔSOH^p , as described in detail in Section V. $\Delta k^p(t)$ and $\Delta d^p(t)$ are derived from the variation in the estimated p^{th} cycle SOC-OCV curve due to ΔSOH^p , while ΔR_i^p is derived from ΔSOH^p based on the functional relationship of R_i^p with SOH^p . ΔSOH^p is obtained by combining the uncertainty involved in the prediction of SOH^p with the variation of predicted SOH^p due to different operational temperature (refer to Tables 1, IIIV and IX). The uncertainty bounds of the remaining parameters, ΔR_t^p , ΔC_{cs}^p and ΔC_{cb}^p , are from the maximum deviations listed in Table 1. Finally, $w_1^p(t)$ and $w_2^p(t)$ are obtained in terms of $\Delta k^p(t)$, $\Delta d^p(t)$, ΔR_t^p , ΔR_{cs}^p , ΔC_{cs}^p , ΔC_{cb}^p and $\Delta I^p(t)$ by applying the first-order Taylor-series expansion to (1), as follows:

$$w_1^p(t) = 1/(k^p(t) c_{cb}^p) [\Delta I^p(t) - (I^p(t) k^p(t) \Delta k^p(t) (I^p(t)/C_{cb}^p) \Delta C_{cb}^p)] \quad (3)$$

$$w_2^p(t) = 1/(R_t^p c_{cb}^p) [(V_{cs}^p/R_t^p) \Delta R_t^p + (V_{cs}^p(t)/C_{cs}^p) \Delta C_{cs}^p] + 1/C_{cs}^p [\Delta I^p(t) - (I^p(t)/C_{cs}^p) \Delta C_{cs}^p].$$

$$w_3^p(t) = \Delta v^p(t) : \text{terminal voltage measurement noise} \quad (4)$$

For an alternative account of temperature in a model, refer to [24] for a battery model with temperature set as a state variable.

B. CPF FOR PROBABILISTIC ANOMALY DETECTION

The CPF was suggested as a unified framework for data fusion in the presence of spurious data [26], [27]. In CPF, the two variables, $x_1 \in \mathbb{R}^n$ and $x_2 \in \mathbb{R}^m$, under fusion are concatenated into a joint variable, x , $x^T = [x_1, x_2]^T$, $x \in \mathbb{R}^{n+m}$, in the fusion space. The constraint manifold, $M(x)$, is then defined in the fusion space as the constraint that should be satisfied by x_1 and x_2 . For instance, we can define $x_1 = [SOC^p(t), V_{cs}^p(t)]^T$ and $x_2 = v^p(t)$ with $M(x)$ defined by (2). Data fusion in the CPF starts by defining the probability distribution of x in the fusion space as the joint probability distribution of x_1 and x_2 . Then, CPF identifies the probability distribution of x on the constraint manifold, $M(x)$, and finds the maximum probability point, x^* , on the constraint manifold as the fused data.

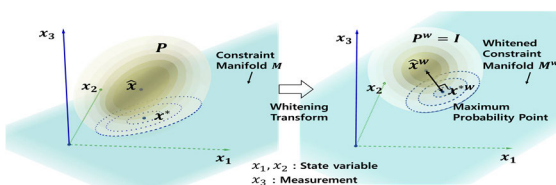


FIGURE 2. Schematic illustration of CPF-based data fusion.

The probability distribution of x around x^* on the constraint manifold represents the uncertainty associated with the fused data, x^* . Refer to Fig. 2 for the illustration of CPF-based data fusion. Note that, if the probability distribution of x is Gaussian and the constraint manifold is linear, the maximum probability point, x^* , and the probability distribution of x on the constraint manifold can be obtained by a well-defined mathematical formula. Consider two Gaussian random variables to be fused, $x_1 \in \mathbb{R}^n$ and $x_2 \in \mathbb{R}^m$, with their means and covariances represented as $\hat{x}_1 \in \mathbb{R}^n$, $P_1 \in \mathbb{R}^{n \times n}$ and $\hat{x}_2 \in \mathbb{R}^m$, $P_2 \in \mathbb{R}^{m \times m}$, respectively. Then, the probability distribution of x , $x = [x_1, x_2]^T$, $x \in \mathbb{R}^{n+m}$, is represented in the fusion space as its mean, \hat{x} , and covariance, P , as follows:

$$\hat{x} = \begin{bmatrix} \hat{x}_1 \\ \hat{x}_2 \end{bmatrix}, P = \begin{bmatrix} P_1 & P_{12} \\ P_{12}^T & P_2 \end{bmatrix} \quad (5)$$

where $P_{12} \in \mathbb{R}^{n \times m}$ represents the cross-covariance between x_1 and x_2 . Now, assume that x_1 and x_2 are subject to a linear constraint denoted by the constraint manifold, $C_1 x_1 = C_2 x_2$. The constraint manifold, $C_1 x_1 = C_2 x_2$, can equivalently be represented as a matrix, M , the columns of which are the basis vectors spanning the constraint manifold. To derive x^* , first, we apply the whitening transformation, W , to x by $x^w = Wx$, such that P in the x space becomes I^w , indicating a unit hypersphere, in the x^w space. W is defined as $W = D^{-1/2} E^T$, with D and E representing the eigenvalue and eigenvector matrices of P , respectively. Then, \hat{x} , P , and M in the x space are transformed into the respective \hat{x}^w , P^w , and M^w in the x^w space by $\hat{x}^w = W\hat{x}$, $P^w = WPW^T = I^w$ and $M^w = WM$. In the x^w space, the maximum probability point, \hat{x}^{w*} , and the covariance, P^{w*} , around \hat{x}^{w*} , on M^w can be obtained simply by projecting \hat{x}^w and I^w onto M^w , as illustrated in Fig. 2. Finally, \hat{x}^* and P^* on M in the original fusion space is obtained, as the fused result of x_1 and x_2 , by applying an inverse whitening transformation, W^{-1} , to \hat{x}^{w*} and P^{w*} , as follows:

$$\hat{x}^* = W^{-1} P_r(M^w) W \hat{x}^w \quad (6)$$

$$P^* = W^{-1} P_r(M^w) P_r(M^w)^T W^{-T} \quad (7)$$

where $P_r(M^w)$ is the projection operator projecting onto the linear constraint manifold, M^w , and is given by:

$$P_r(M^w) = M^w (M^{wT} M^w)^{-1} M^{wT} \quad (8)$$

By applying (8) and the following relationships,

$$P = EDE^T \text{ and } P^{-1} = ED^{-1}E^T \quad (9)$$

$$W^T W = ED^{-1}E^T = P^{-1} \quad (10)$$

to (6) and (7), the final fused estimate, \hat{x}^* and P^* , can be derived by

$$\hat{x}^* = M (M^T P^{-1} M)^{-1} M^T P^{-1} \hat{x} \quad (11)$$

$$P^* = M (M^T P^{-1} M)^{-1} M^T \quad (12)$$

In anomaly detection, the weighted distance, q , from the fused estimate \hat{x}^* to the original vector \hat{x} , $q = (\hat{x} - \hat{x}^*)^T P^{-1} (\hat{x} - \hat{x}^*)$, serves as a probabilistic anomaly indicator. Specifically, q follows a chi-squared distribution with $(n + m)$ degrees of freedom (DOF), $q \sim \chi^2(n + m)$, where $(n + m)$ indicates the dimension of the fusion space. With $q \sim \chi^2(n + m)$, we can assign a threshold, q_α , such that, if q is less than q_α , we decide, with the statistical confidence of $100(1 - \alpha)\%$, $\alpha \in (0, 1)$, that \hat{x} is an inlier of \hat{x}^* . Formally, the following hypothesis test is performed for anomaly detection:

Hypothesis H_0 : \hat{x} represents no anomaly.

Decision Rule: accept H_0 if $q < q_\alpha \sim \chi^2(n + m)$ and reject H_0 if $q \geq q_\alpha \sim \chi^2(n + m)$

To obtain q_α for the given significance level, α , with the given DOF, refer to the Chi-square distribution table [29].

III. OVERALL FLOW OF THE PROPOSED ANOMALY DETECTION SYSTEM

The overall flow of the proposed anomaly detection system is presented here together with the flow diagram shown in Fig. 3 for clarity.

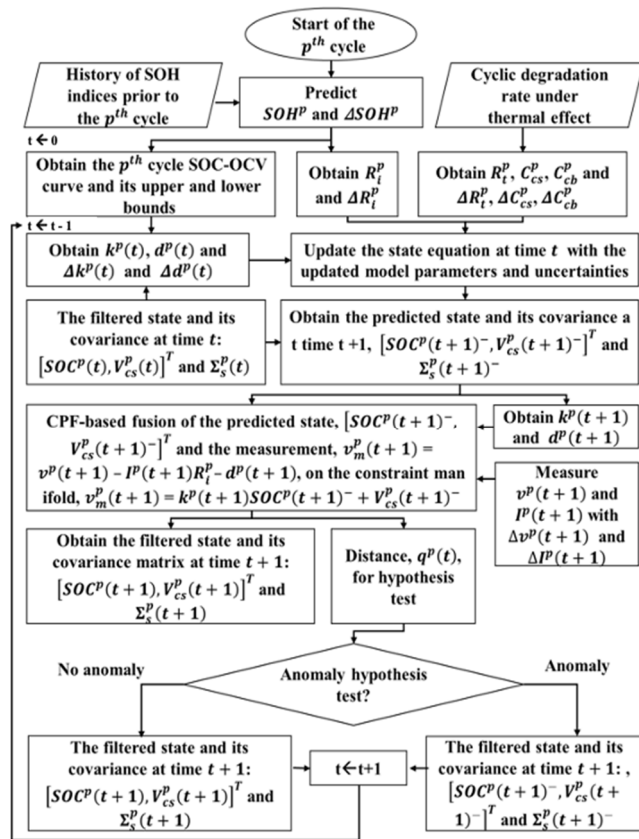


FIGURE 3. An overall flow of the proposed anomaly detection system. Note: the superscript “-” represents a “predicted” value “before” filtering by CPF.

Overall, the proposed system is comprised of the following five steps of processes: 1) At the start of the p^{th} cycle, SOH^p and its uncertainty, ΔSOH^p , are first predicted. Then,

the p^{th} cycle model parameters, $R_i^p, R_t^p, C_{cs}^p, C_{cb}^p$, and their uncertainties, $\Delta R_i^p, \Delta R_t^p, \Delta C_{cs}^p, \Delta C_{cb}^p$, as well as the p^{th} cycle SOC-OCV curve and its uncertainty are derived based on SOH^p and ΔSOH^p . 2) At time t , first, the filtered state and its covariance at time $(t-1)$, $[SOC^p(t-1), V_{cs}^p(t-1)]^T$ and $\Sigma_s^p(t-1)$, are propagated to the predicted state and its covariance, $[SOC^p(t)^-, V_{cs}^p(t)^-]^T$ and $\Sigma_s^p(t)^-$, at time t based on the state equation at time $(t-1)$. The state equation at time $(t-1)$ is obtained from (1), (2), and (3) by deriving $k^p(t-1), d^p(t-1), \Delta k^p(t-1)$, and $\Delta d^p(t-1)$ from the p^{th} cycle SOC-OCV curve and its uncertainty. 3) Then, the predicted state, $[SOC^p(t)^-, V_{cs}^p(t)^-]^T$, and the measured terminal voltage, $v^p(t)$, at time t undergo the CPF-based data fusion in their joint space, x , to generate the filtered state and its covariance, $[SOC^p(t), V_{cs}^p(t)]^T$ and $\Sigma_s^p(t)$, at time t . 4) In the process of fusing $[SOC^p(t)^-, V_{cs}^p(t)^-]^T$ and $v^p(t)$, the probabilistic anomaly indicator, $q^p(t)$, representing the distance from the joint vector $\hat{x}(t)$, $\hat{x}(t) = [SOC^p(t)^-, V_{cs}^p(t)^-, v^p(t)]^T$, to the fused vector, $\hat{x}^*(t)$, is computed based on $q^p(t) = (\hat{x} - \hat{x}^*)^T P^{-1} (\hat{x} - \hat{x}^*)$, where P is obtained by $\Sigma_s^p(t)^-$ and $w_3^p(t)$. Then, applying the statistical hypothesis test described in Section II-B to $q^p(t)$, whether or not an anomaly is present at time t is decided. 5) Finally, the process iterates from time t to time $t + 1$ based on the following conditional flow: If no anomaly is detected at time t , the process advances to time $t + 1$ by moving to step 2). On the other hand, if an anomaly is detected at time t , the predicted state and its covariance, $[SOC^p(t)^-, V_{cs}^p(t)^-]^T$ and $\Sigma_s^p(t)^-$, replace the filtered state and its covariance, $[SOC^p(t), V_{cs}^p(t)]^T$ and $\Sigma_s^p(t)$, at time t to advance to time $t + 1$. This conditional flow is intended to keep the battery model to represent only the normal aging behavior of a battery by deleting influences from abnormal behaviors, which helps to enhance sensitivity in detecting a slow mode of anomalies. Note that, in Fig. 3, $v_m^p(t), v_m^p(t) = v^p(t) - I^p(t)R_i^p - d^p(t)$, is introduced as a means of having the constraint manifold linear: $v_m^p(t) = [k^p(t), 1][SOC^p(t)^-, V_{cs}^p(t)^-]^T$ (Refer to Section VI for more details).

IV. ONLINE REAL-TIME SOH PREDICTION UNDER LOAD CURRENT VARIATIONS AND NON-STANDARD PRACTICES

SOH prediction of rechargeable batteries can be conducted based on either charging or discharging cycles. Here, we present a deep-learning approach to SOH prediction based on a cyclic history of terminal voltage and current profiles for charging and discharging [30]. In particular, the proposed SOH prediction accounts for nonstandard charging and discharging practices in real-world operations, as well as the intracycle variation of load current [31]. By nonstandard charging and discharging practices, we mean less than full charging and discharging between the lower and upper cutoff voltages set as a standard. As described, the predicted SOH will be used for cyclic as well as temporal updates of model parameters to trace the normal aging behavior of batteries.

A. INPUT FEATURE INDICES FOR SOH PREDICTION

For SOH prediction, we define four SOH indices extracted from terminal voltage and current profiles as the input features to the proposed deep-learning network. The four indices were selected to work well with varying load currents and nonstandard practices. The four indices defined are 1) the total charge charged or discharged during a cycle, 2) the entropy of a voltage profile during charging or discharging, 3) the average of load current during a cycle, and 4) the standard deviation of load current during a cycle. Notably, the third and fourth indices are specifically chosen to address variations in load current.

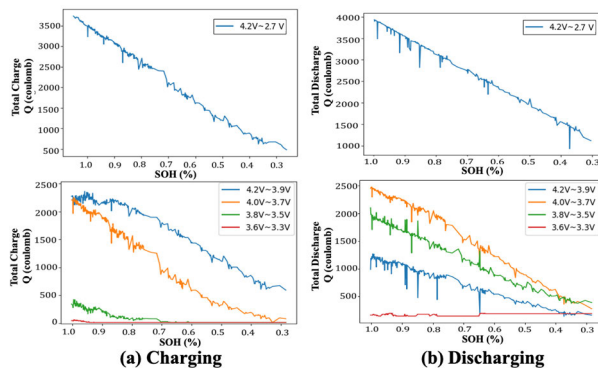


FIGURE 4. The variation of the total charge, Q , with respect to SOH degradation for charging (a) and discharging (b) under standard (upper) and nonstandard (lower) practices.

1) TOTAL CHARGE INDEX

The total-charge index, Q , is obtained by integrating the terminal current during a charging or discharging cycle, regardless of whether the standard or nonstandard practice is involved. Fig. 4 shows the variation of Q along SOH degradation for charging (a) and discharging (b) with constant load currents and under standard (upper) and nonstandard (lower) practices. Fig. 4 is produced based on the custom-collected data using a 3.25Ah lithium-ion battery INR18650. Fig. 4 depicts that Q is strongly correlated with SOH for both charging and discharging unless nonstandard practices take such extreme voltage ranges as 3.3V-3.6V (red) and 3.5V-3.8V (green) for charging while 3.3V-3.6V (red) for discharging. Note that, in Section VII-B, we provide the minimum voltage ranges that must be covered by charging and discharging to ensure adequate accuracy in SOH prediction under nonstandard practices.

2) VOLTAGE-TIME ENTROPY INDEX

The voltage-time entropy index, VE, is defined as the entropy of the voltage derivative of time, dt/dv , associated with a voltage profile. In practice, VE is obtained by equally dividing the range of charging or discharging voltage into a fixed number of voltage segments, v_i , $i = 1, \dots, M$, and assign probabilities to individual segments, $p(v_i)$, $i = 1, \dots, M$, in proportion to their corresponding time intervals.

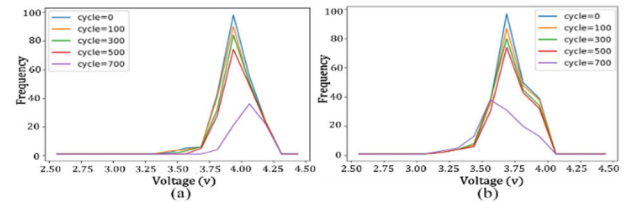


FIGURE 5. The variation of dt/dv probability distribution, $p(v_i)$, $i = 1, \dots, M$, along cyclic aging for charging (a) and discharging (b).

Fig. 5 exemplifies typical variations of $p(v_i)$, $i = 1, \dots, M$, distribution along cyclic aging for charging (a) and discharging (b) with $M = 17$. Based on $p(v_i)$, $i = 1, \dots, M$, the voltage-time entropy, VE, is obtained by

$$VE = - \sum_{i=1}^M p(v_i) \log_{10} p(v_i). \quad (13)$$

Fig. 6 demonstrates the correlation existing between VE and SOH for charging (a) and discharging (b) with constant load currents and under standard (upper) and nonstandard (lower) practices of various voltage ranges.

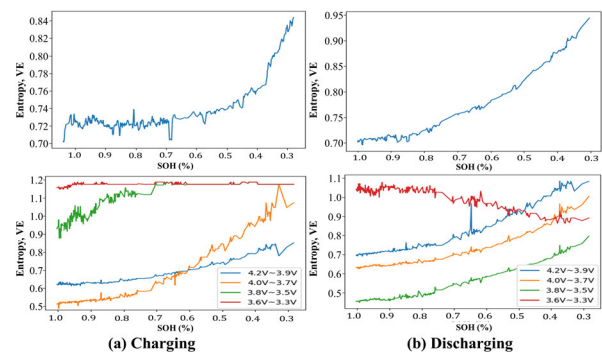


FIGURE 6. The variation of voltage-time entropy, VE, with respect to SOH degradation for charging (a) and discharging (b) under standard (upper) and non-standard (lower) practices.

In Fig. 6, a clear relationship between VE and SOH is indicated for charging and discharging unless nonstandard practices take such extreme voltage ranges as 3.3V-3.6V (red) and 3.5V-3.8V (green) for charging while 3.3V-3.6V (red) for discharging.

3) LOAD CURRENT AVERAGE AND STANDARD DEVIATION INDICES

To account for the impact of inter-cycle and intracycle variations of load current on SOH degradation, we add to Q and VE the third and fourth SOH indices: the cyclic average, I_m , and standard deviation, SD, of load current. Fig. 7 depicts how different values of I_m and SD indices affect Q (left) and VE (right) vs. SOH in the case of discharging. Fig. 7 is custom-generated based on five 3.25Ah lithium-ion INR18650 batteries. Fig. 7 indicates that both I_m and SD affect the Q and VE relationships with SOH. For instance, although the blue and purple have the same I_m of 1.6A, their Q and VE relationships with SOH are not the same with their different SDs of 0 and 0.92, respectively.

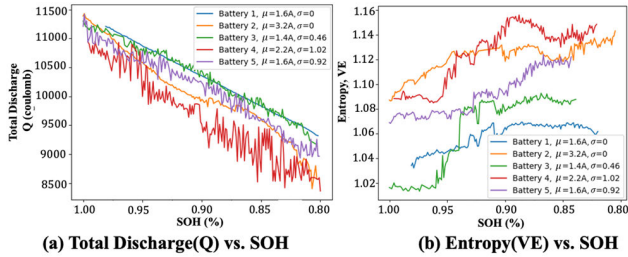


FIGURE 7. The variation in Q vs. SOH (a) and VE vs. SOH (b) under load current variations denoted by average ($\mu = I_m$) and standard deviation ($\sigma = SD$).

B. STACKED LSTM FOR SOH PREDICTION WITH FOUR INDICES

The prediction of SOH at the p^{th} cycle, SOH^p , is based on a sequence of k input vectors, $[u^{p-k}, u^{p-k+1}, \dots, u^{p-1}]$, where u^{p-j} , $j=1, \dots, k$, is a vector composed of the four SOH indices at the $(p-j)^{th}$ cycle: $u^{p-j} = [Q^{p-j}, VE^{p-j}, I_m^{p-j}, SD^{p-j}]^T$. Note that, in the case where the load current is constant, e.g., charging under constant current, then, SD^{p-j} is set to null. As shown in Fig. 8, we adopted a stacked LSTM [32] for SOH prediction that consists of two LSTM layers and a fully-connected layer. A stacked configuration is chosen for enhancing performance beyond a single-layer configuration. Each layer of the LSTM stack is made up of k LSTM units connected to their neighboring units to represent a sequence of k input vectors.

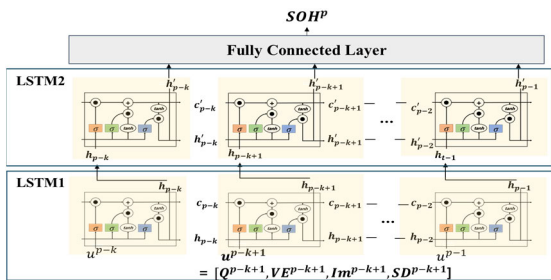


FIGURE 8. A two-layer stacked LSTM with a fully-connected output layer designed for SOH prediction at the p^{th} cycle.

The $(p-j)^{th}$ LSTM unit, $j = 1, \dots, k$, in the first and second layers is governed by typical LSTM formula in terms of the respective cell states, C_{p-j} and C'_{p-j} , as well as hidden states, h_{p-j} and h'_{p-j} with their associated input, output and forget gates [29]. The fully-connected layer receives all the outputs from the second layer of the LSTM stack and uses them as its input to output SOH^p . On the other hand, ΔSOH^p is obtained by combining the uncertainties involved in the LSTM-based SOH^p prediction (refer to Section VII-B) with the possible deviations from the predicted SOH^p due to operational temperatures (refer to Table 1). The proposed LSTM stack is implemented with the length of the input sequence, k, set to 20, while the values of four input indices, Q, VE, I_m , and SD , are normalized so that their values lie

between 0 and 1. To avoid overfitting in training, a dropout is applied between the LSTM stack and the fully connected layer with a dropout rate of 0.3. Also, the Adam optimizer is used for adjusting the learning rate along the progress of training for optimal convergence while avoiding falling into local minima.

C. EQUIVALENT TRANSFORMATION OF SOH INDICES FROM NONSTANDARD TO STANDARD

Since the proposed SOH prediction takes account of non-standard practices, the input sequence to a stacked LSTM should include Qs and VEs from a mixture of standard and nonstandard practices. However, the mixture of standard and nonstandard practices in the input to the proposed LSTM stack raises the following problem. 1) Since different Qs and VEs from nonstandard voltage ranges can correspond to the same SOH, as indicated by Figs. 4 and 6, (Q, VE) needs to be augmented into (V_1, V_2, Q, VE) by concatenating its associated voltage range, V_1 and V_2 , to make it unique as an input. 2) Due to the random nature of the cycles and voltage ranges by which nonstandard practices occur, the amount of data required to represent the input sequence may be subject to a combinatorial explosion, making network training difficult to implement. To solve the above issue, we propose the following: 1) Establishment of the minimum voltage ranges in charging and discharging that are required for the derived Q and VE to be effective as SOH indicators (refer to Section VII-B). 2) Transformation of $(V_1, V_2, Q, VE)^n$ from the non-standard practice to the equivalent $(Q, VE)^s$ from the standard practice in such a way that that the same SOH corresponds to $(V_1, V_2, Q, VE)^n$ and $(Q, VE)^s$. For (V_1, V_2) covering the minimum voltage range, the transformed $(Q, VE)^s$ is then used in the input sequence for SOH prediction, instead of $(V_1, V_2, Q, VE)^n$. Otherwise, the cycle with (V_1, V_2) failed in the minimum coverage is skipped in the input sequence. Here, a deep regression network with a fully-connected configuration performs the equivalence transformation, as shown in Fig. 9. Refer to Section VII-B and C for experimental verification of the effectiveness of the proposed regression network for SOH prediction.

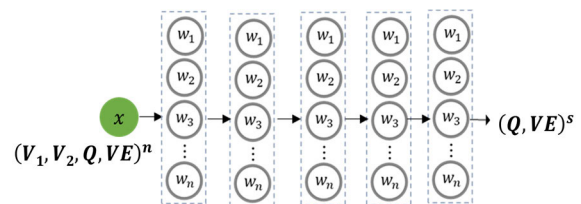


FIGURE 9. The proposed regression network with a fully-connected configuration to learn the transformation from $(V_1, V_2, Q, VE)^n$ to $(Q, VE)^s$.

The proposed regression network is trained by using the root-mean-square-error (RMSE) as the loss function while Adam Optimizer is adopted for adjusting the learning rate along the progress of training for optimal convergence.

V. SOH-BASED ESTIMATION OF AGING MODEL PARAMETERS: $k^p(t)$, $d^p(t)$ AND R_i^p

A. ESTIMATION OF R_i^p FROM SOH^p

The internal resistance, R_i^p , is known to have a linear relationship with SOH^p , as expressed in the following [33]:

$$R_i^p = c_1 \cdot SOH^p + c_2. \quad (14)$$

To obtain c_1 and c_2 , we experimentally obtained the voltage drops at a number of discharge cycles for the battery INR18650 and applied linear least-square regression to obtain -0.0357 and 0.17 for c_1 and c_2 , respectively. The uncertainty bound of R_i^p , ΔR_i^p , was then obtained by:

$$\Delta R_i^p = c_1 \cdot \Delta SOH^p + c_2. \quad (15)$$

B. ESTIMATION OF $k^p(t)$ AND $d^p(t)$ BASED ON $SOC^p(t) - OCV^p(t)$ CURVE DERIVED FROM SOH^p

The estimation of $k^p(t)$ and $d^p(t)$ starts with deriving $SOC^p(t) - OCV^p(t)$ curve at the p^{th} cycle based on the predicted SOH^p . Since, from (2), the $SOC^p(t) - OCV^p(t)$ curve is represented by $OCV^p(t) = k^p(t)SOC^p(t) + d^p(t)$, $k^p(t)$ and $d^p(t)$ can be estimated from the $SOC^p(t) - OCV^p(t)$ curve as the tangential slope and $OCV^p(t) - k^p(t)SOC^p(t)$, respectively, at the time t . The $SOC^p(t) - OCV^p(t)$ curve can be obtained from a reference $SOC^r(t) - OCV^r(t)$ curve collected at the initial cycle with the maximum charge capacity, Q_r . $OCV^r(t)$ is achieved by averaging the discharging and charging terminal voltage profiles obtained based on the same constant current for both, as illustrated in Fig. 10. The maximum battery charge capacity, Q_r , is then obtained by integrating the discharging current for the duration of the cut-off time T_r , i.e., the duration between the upper and lower cutoff voltages.

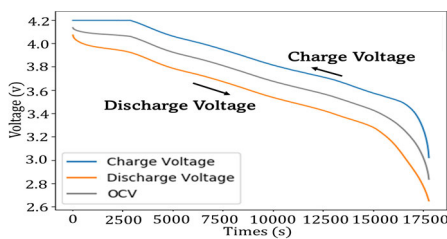


FIGURE 10. The reference OCV curve was obtained by averaging the discharging and charging terminal voltages produced from the same constant current (0.7 A) discharging and charging at the initial cycle (obtained from a real battery, INR18650).

Based on $OCV^r(t)$ and Q_r , $OCV^p(t)$ is obtained by the following steps [32]: 1) Compute the cut-off time T_p at the p^{th} cycle by $T_r \times Q_p / Q_r$, where Q_p represents the maximum charge capacity at the p^{th} cycle and is obtained from the predicted SOH^p . 2) Generate $OCV^p(t)$ from $OCV^r(t)$ in such a way that $OCV^p(t_k) = OCV^r(t_r)$ for $t_r \in T_r$ and $t_k = t_r \times Q_k / Q_r$. Fig. 11 (a) shows $OCV^p(t)$ (orange) generated from $OCV^r(t)$ (blue) based on the above steps when SOH^p is 0.9. On the other hand, $SOC^p(t)$ is a decreasing function from

Q_p / Q_r , the rate of which is determined by the discharging current. Fig.11 (b) illustrates $SOC^p(t)$ for the case of a constant discharging current.

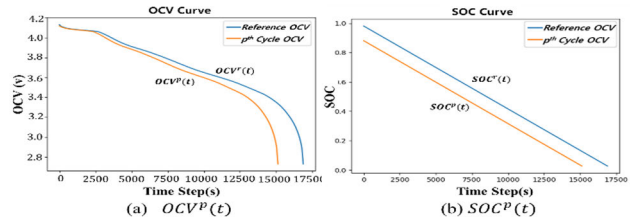


FIGURE 11. (a) $OCV^p(t)$ (orange) generated from $OCV^r(t)$ (blue) based on SOH^p of 0.9. (b) $SOC^p(t)$ (orange) under a constant discharging current.

Now, the $SOC^p(t) - OCV^p(t)$ curve at the p^{th} cycle is produced by relating the $OCV^p(t)$ with $SOC^p(t)$ thus obtained, as shown in Fig. 12 (b). Finally, $k^p(t)$ and $d^p(t)$ are derived from the $SOC^p(t) - OCV^p(t)$ curve based on the tangential slope and $OCV^p(t) - k^p(t)SOC^p(t)$, respectively, at the time t , as illustrated in Fig. 13.

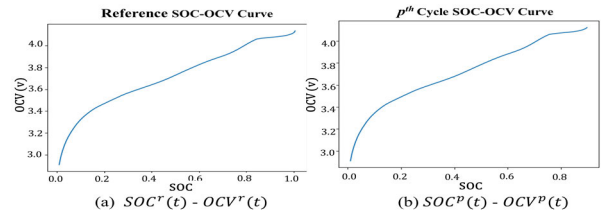


FIGURE 12. (a) $SOC^r(t) - OCV^r(t)$ and (b) $SOC^p(t) - OCV^p(t)$ curves generated from the initial SOH and SOH^p , respectively.

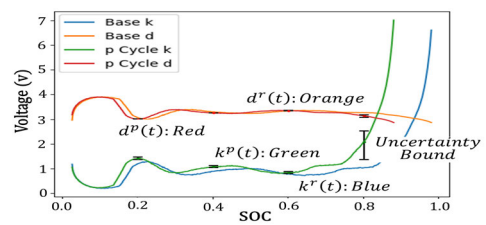


FIGURE 13. $k^p(t)$ (green) and $d^p(t)$ (red) derived from the $SOC^p(t) - OCV^p(t)$ curve in Fig. 12(b) as well as $k^r(t)$ (blue) and $d^r(t)$ (orange) derived from the $SOC^r(t) - OCV^r(t)$ curve in Fig.12(a).

$\Delta k^p(t)$ and $\Delta d^p(t)$ are obtained by deriving $(k^p(t)^+, d^p(t)^+)$ and $(k^p(t)^-, d^p(t)^-)$ that correspond, respectively, to $SOH^p + \Delta SOH^p$ and $SOH^p - \Delta SOH^p$ such that $\Delta k^p(t) = |k^p(t)^+ - k^p(t)^-|$ and $\Delta d^p(t) = |d^p(t)^+ - d^p(t)^-|$.

VI. DISCRETE-TIME IMPLEMENTATION OF CPF-BASED ANOMALY DETECTION

In the implementation, the continuous-time state and measurement equations, (1) and (2), are converted into the discrete-time equations with the sampling interval of T ,

as follows:

$$x_1^p(k)^- = \begin{bmatrix} 1 & 0 \\ 0 & 1 - \frac{T}{C_{cs}^p R_i^p} \end{bmatrix} x_1^p(k-1) + \begin{bmatrix} \frac{T}{k^p(k-1)C_{cb}^p} \\ \frac{T}{C_{cs}^p} \end{bmatrix} I^p(k-1) + \begin{bmatrix} Tw_1^p(k-1) \\ Tw_2^p(k-1) \end{bmatrix} \quad (16)$$

$$v^p(k) = [k^p(k) \ 1] x_1^p(k)^- + I^p(k) R_i^p + d^p(k) + w_3^p(k) \quad (17)$$

Note that the superscript “-” in $x_1^p(k)^-$, $x_1^p(k)^- = [SOC^p(k)^-, V_{cs}^p(k)^-]^T$, represents the “predicted” state at time k before turning into the “filtered” state $x_1^p(k)$, $x_1^p(k) = [SOC^p(k), V_{cs}^p(k)]^T$. The filtered state, $x_1^p(k)$, and its covariance matrix, $\Sigma_1^p(k)$, are derived in the process of fusing $x_1^p(k)^-$ and its covariance matrix, $\Sigma_1^p(k)^-$, with the measured terminal voltage, $v^p(k)$. As described in Section III, we define a new variable, $x_2^p(k)$, $x_2^p(k) = v^p(k) I^p(k) R_i^p + d^p(k)$, based on (17) such that the CPF fusion takes place between $x_1^p(k)^-$ and $x_2^p(k)$, instead of $v^p(k)$, with the linear constraint manifold expressed by

$$x_2^p(k) = [k^p(k) \ 1] x_1^p(k)^- \quad (18)$$

$x_1^p(k)^-$ and $\Sigma_1^p(k)^-$ are predicted by propagating the respective $x_1^p(k-1)$ and $\Sigma_1^p(k-1)$ based on (16). Specifically, $\Sigma_1^p(k)^-$ can be computed by the following equation with E denoting the expected value:

$$\Sigma_1^p(k)^- = \begin{bmatrix} 1 & 0 \\ 0 & 1 - \frac{T}{C_{cs}^p R_i^p} \end{bmatrix} \Sigma_1^p(k-1) \begin{bmatrix} 1 & 0 \\ 0 & 1 - \frac{T}{C_{cs}^p R_i^p} \end{bmatrix}^T + E [Tw_1^p(k-1), Tw_2^p(k-1)]^T \times [Tw_1^p(k-1), Tw_2^p(k-1)], \quad (19)$$

For the second part of (19), the cross-covariance between $w_1^p(k-1)$ and $w_2^p(k-1)$ is obtained by simulating their joint distribution based on (3) and (4). On the other hand, the covariance matrix, $\Sigma_2^p(k)$, representing the uncertainty of $x_2^p(k)$ is obtained based on $E[\Delta x_2^p(k)^2]$, where $\Delta x_2^p(k)$ consists of the noise involved in the measured terminal voltage and current at the time k , $w_3^p(k)$ and $\Delta I^p(k)$, respectively, and the uncertainty bounds involved in model parameters, ΔR_i^p , $\Delta d^p(k)$ and $\Delta k^p(k)$, as follows:

$$\Delta x_2^p(k) = w_3^p(k) - \Delta I^p(k) R_i^p - I^p(k) \Delta R_i^p - \Delta d^p(k) - \Delta k^p(k) x_1^p(k)^- \quad (20)$$

Note that in the last term, $\Delta k^p(k) x_1^p(k)^-$, in $\Delta x_2^p(k)$ is intended to make the constraint manifold noise-free. $E[\Delta x_2^p(k)^2]$ is then obtained by simulating the distribution of $\Delta x_2^p(k)$ based on the uncertainty bounds involved in (20). With the above derivations, CPF fusion of $x_1^p(k)^-$ and $x_2^p(k)$ can now be performed for anomaly hypothesis testing at the time k . First, $x_1^p(k)^-$ and $x_2^p(k)$ are jointly represented as a joint vector, $\hat{x}^p(k)^-$, and its covariance matrix, $\hat{\Sigma}^p(k)^-$, in the fusion space, while the linear constraint manifold, (18),

is denoted as the independent basis vectors, $M^p(k)$, spanning the manifold:

$$\hat{x}^p(k)^- = \begin{bmatrix} \hat{x}_1^p(k)^- \\ \hat{x}_2^p(k) \end{bmatrix} \text{ and } \hat{\Sigma}^p(k)^- = \begin{bmatrix} \Sigma_1^p(k)^- & 0 \\ 0 & \Sigma_2^p(k) \end{bmatrix} \quad (21)$$

$$M^p(k) = \begin{bmatrix} 1 & 0 \\ 0 & 1 \\ k^p(k) & 1 \end{bmatrix}. \quad (22)$$

Then, based on (11) and (12), the filtered joint vector, $\hat{x}^p(k)$, and its covariance matrix, $\hat{\Sigma}^p(k)$, at time k are obtained by:

$$\hat{x}^p(k) = M^p(k) \left[M^p(k)^T (\hat{\Sigma}^p(k)^-)^{-1} M^p(k) \right]^{-1} M^p(k)^T (\hat{\Sigma}^p(k)^-)^{-1} \hat{x}^p(k)^- \quad (23)$$

$$\hat{\Sigma}^p(k) = M^p(k) \left[M^p(k)^T (\hat{\Sigma}^p(k)^-)^{-1} M^p(k) \right]^{-1} M^p(k)^T. \quad (24)$$

From $\hat{x}^p(k)$ and $\hat{\Sigma}^p(k)$ derived by (23) and (24), we can extract the filtered state, $x_1^p(k)$, and covariance matrix, $\Sigma_1^p(k)$, for use in the next iteration of prediction, filtering, and anomaly detection at the time $k+1$.

As discussed in Section II-B, the consistency test for anomaly detection is based on the uncertainty-weighted distance, $q^p(k)$, between the predicted joint vector, $\hat{x}^p(k)^-$, and the filtered joint vector, $\hat{x}^p(k)$, in the fusion space:

$$q^p(k) = [\hat{x}^p(k)^- - \hat{x}^p(k)]^T \hat{\Sigma}^p(k)^{-1} [\hat{x}^p(k)^- - \hat{x}^p(k)] \quad (25)$$

Formally, the following hypothesis test is formulated:

Hypothesis H_0 : $\hat{x}^p(k)^-$ represents no anomaly.

Decision: Accept H_0 if $q^p(k) < q_\alpha \sim \chi^2(3)$,

Reject H_0 if $q^p(k) \geq \tilde{A}q_\alpha \sim \chi^2(3)$

The threshold, q_α , is defined in such a way that $P_r\{q^p(k) \geq q_\alpha\} = \alpha$, which ensures that $\hat{x}^p(k)^-$ and $\hat{x}^p(k)$ are consistent with the statistical confidence of $100(1-\alpha)\%$. To obtain the critical value, q_α , for the chosen significance level, α , refer to the Chi-square test table [34]. Note that, in the case where the anomaly is detected at the time k , $\hat{x}_1^p(k)$ and $\Sigma_1^p(k)$ are substituted by $\hat{x}_1^p(k)^-$ and $\Sigma_1^p(k)^-$ to continue supplying a reference for normal aging to the subsequent iteration, so as to deal with a slow mode of anomalies while avoiding detection errors.


VII. EXPERIMENTAL RESULTS

A. EXPERIMENT SETTING

For the experiment, we employed the custom dataset collected with the 3.25Ah lithium-ion battery INR-18650 together with the publicly available CS-2 family of the CALCE dataset [28]. Refer to Table 2 for the specification of the INR-18650 battery we used.

A total of 3 custom datasets were obtained by repeating charging and discharging cycles over the battery life cycle. We used the battery testing equipment illustrated in Fig. 14

TABLE 2. Specifications of battery INR-18650 used for collecting custom-datasets.

INR-18650	Item	Specification
	Rated Capacity	3250 mAh
	Charge Voltage	4.2 V
	Discharge Cut-off Voltage	2.65 V
	C_{cs}	90 F
	C_{cb}	12240 F
	R_t	0.06 m Ω
	R_i	$0.17 - (0.0357 \times SOH)$ m Ω

**FIGURE 14.** The experimental testbed was used to collect custom datasets with the lithium-ion battery INR-18650 for evaluating the proposed SOH prediction and anomaly detection system.

for data collection. The 3 custom datasets, labeled, respectively, as R1, R2, and R3 datasets were particularly aimed at gathering data under intracycle load current variations. Particularly, we selected the discharging current randomly at the time k based on Gaussian distribution with different mean-standard deviation, (I_m , SD), combinations: (1.4A, 0.46A) for R1, (2.2A, 1.02A) for R2, and (1.6A, 0.92A) for R3 datasets, while maintaining a constant charging current of 1.6A across all 3 datasets. On the other hand, the CS-2 family of CALCE datasets offers life cycle charging and discharging data for the 1.1Ah lithium-ion battery cells under constant discharging currents. Among 6 Types of datasets in the CS-2 family, we adopted Type 1 (CS2-8 and CS2-21), Type 2 (CS2-35 and CS2-36), and Type 3 (CS2-3) datasets for supplementing the custom datasets. Type 1 and Type 2 datasets are based on the constant discharging current of 0.55A and 1.1A, respectively, whereas the Type 3 dataset is based on cyclically alternating constant currents of 0.11, 0.22, 0.55, 1.1, 1.65, and 2.2A. Nevertheless, the charging data of the CS-2 family are based on the standard charging profile with a constant current of 0.55A. For more details on the CS-2 family of CALCE datasets, refer to the ‘‘Battery Data Set. CALCE [28],’’ provided by the CALCE Battery Research Group of the University of Maryland, USA.

B. PERFORMANCE OF SOH PREDICTION UNDER LOAD CURRENT VARIATIONS

The effectiveness of the proposed LSTM stack-based SOH prediction is assessed under the variations in intracycle discharging currents. The performance of the SOH prediction is measured by the root-mean-square-error (RMSE) and the

goodness-of-fit, R^2 , metrics defined as follows:

$$RMSE = \sqrt{\frac{1}{m} \sum_{i=1}^m (y_i - \hat{y}_i)^2} \quad (26)$$

$$R^2 = 1 - \frac{\sum_{i=1}^m (y_i - \hat{y}_i)^2}{\sum_{i=1}^m (y_i - \bar{y})^2} \quad (27)$$

where y_i and \hat{y}_i are, respectively, the ground truth and the predicted SOH at the i^{th} cycle, whereas $\bar{y} = \frac{1}{m} \sum_{i=1}^m y_i$. R^2 is introduced here to assess the regression performance in SOH prediction.

TABLE 3. RMSE and R^2 performance of the proposed SOH prediction evaluated by the CALCE dataset.

Data (CALCE)	Training	Testing	Charging		Discharging	
			RMSE	R^2	RMSE	R^2
Type1 (0.55A) + Type2 (1.1A)	CS2-8 + CS2-35	CS2-21 (0.55A)	0.06063	0.95565	0.02659	0.99213
		CS2-36 (1.1A)	0.01065	0.99739	0.00779	0.99855
Type1 (1.1A)	Type1 + Type2 (60%)	Type1 (40%)	0.02058	0.99082	0.01733	0.99493
		Type2 (40%)	0.01808	0.99183	0.01590	0.99364
Type3 (Alternate)	Type3 (60%)	Type3 (40%)	0.00566	0.99285	0.00805	0.99039
Type1 (0.55A) + Type2 (1.1A) + Type3 (Alternate Currents)	Type1 + Type2 + Type3 (60%)	Type1 (40%)	0.02085	0.99089	0.01793	0.99367
		Type2 (40%)	0.01981	0.99251	0.01593	0.99410
		Type3 (40%)	0.00763	0.98425	0.00709	0.98844
		CS2-8 + CS2-21	0.05211	0.95767	0.02267	0.98707
Type3 (60%)	Type3 (40%)	CS2-35 + CS2-36	0.01394	0.99604	0.00865	0.99819
		Type3 (40%)	0.00596	0.98810	0.00739	0.99147

TABLE 4. RMSE and R^2 performance of the proposed SOH prediction under randomly varying load currents.

Data (Custom)	Training	Testing	Charging		Discharging	
			RMSE	R^2	RMSE	R^2
Random Current with Different (I_m , SD)	R1 (60%)	R1 (40%)	0.00521	0.9605	0.00395	0.9602
	R2 (60%)	R2 (40%)				
	R3 (60%)	R3 (40%)				
	R1+R2+R3 (60%)	R1+R2+R3 (40%)	0.00626	0.9411	0.00525	0.9300
	R1 + R2	R3	0.0068	0.9537	0.00449	0.9632
R2 + R3	R1					
	R3 + R1	R2				

The proposed LSTM stack for SOH prediction was evaluated based on the CALCE and custom datasets, which allows for assessing the differences in prediction performance due to constant (CALCE) and random (custom dataset) intracycle load currents, as summarized in Tables 3 and 4 obtained for the CALCE and custom datasets, respectively. Furthermore, the tables include the performance of both charging-based and discharging-based SOH predictions for their comparative analysis. Especially, we configured various combinations of training and testing datasets to assess the

robustness of the proposed SOH prediction against data configurations. As shown in Tables 3 and 4, the training and testing columns list various configurations of training and testing datasets with each row indicating a particular configuration of training and testing datasets. A non-overlapping division between training and testing datasets was obtained either by assigning independent datasets to train and test separately or by randomly dividing the same datasets into two non-overlapping datasets with a predefined division percentile. The symbol + is used to represent the union of datasets. Note that not only Tables 3 and 4 but also all the tables presented in Section VII follow the same data configuration as well as notational convention principles as described above for Tables 3 and 4. Table 3 depicts that the proposed LSTM stack-based SOH prediction performs well with the CALCE dataset for both charging-based and discharging-based SOH predictions. In particular, the RMSE errors and R^2 scores for different testing cases are, on average, 0.0140 and 0.9929, respectively, for discharging and 0.0214 and 0.9852, respectively, for charging, which are comparable to other state-of-the-art performances reported to date [19], [25].

Table 4 illustrates the performance of the proposed SOH prediction under randomly varying load currents with different combinations of R1, R2, and R3 datasets configured for training and testing. The RMSE errors and R^2 scores for different testing cases are, on average, 0.0045 and 0.9511, respectively, for discharging and 0.0061 and 0.9517, respectively, for charging. This shows that the proposed SOH prediction, with I_m and SD presented in the input indices, performs equally as well under randomly varying load currents as that under constant load currents. To analyze the significance of having SD as an input index in SOH prediction under varying load currents, we repeated the same experiment as done for Table 4 except for setting SD=0 in the input sequence. The result is summarized in Table 5. Table 5 depicts that, without SD, the RMSE and R^2 scores become, on average, 0.0122 and 0.9043, respectively, which denotes a significant degradation in performance from the RMSE and R^2 of 0.0045 and 0.9511, respectively, with SD.

TABLE 5. RMSE and R^2 performance of the proposed SOH prediction under random load currents with SD=0.

Data (Custom)	Training	Testing	Discharging	
			RMSE	R^2
Random Current with Different ($I_m, SD=0$)	R1 (60%)	R1 (40%)	0.01016	0.9137
	R2 (60%)	R2 (40%)		
	R3 (60%)	R3 (40%)		
	R1+R2+R3 (60%)	R1+R2+R3 (40%)	0.00859	0.9383
	R1 + R2	R3	0.01762	0.8610
	R2 + R3	R1		
R3 + R1	R2			

Tables 3 and 4 also show that the performance of discharging-based SOH prediction is somewhat better than

that of charging-based SOH prediction for both constant and random load current cases. Also, in Table 3, the SOH prediction performance with CS2-21 as the testing dataset is shown a lot worse than that with CS2-36. This signifies the variance in aging behaviors among cells of the same model, verifying the need for robust SOH prediction under cell sampling.

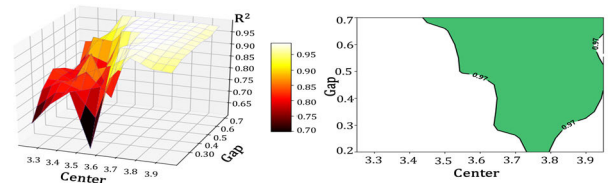


FIGURE 15. The green zone (b) represents the required minimum voltage range for discharging, inside which R^2 performance (a) is 0.97 and higher.

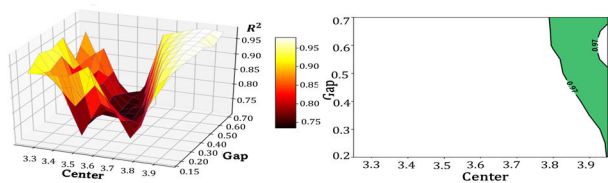


FIGURE 16. The green zone (b) represents the required minimum voltage range for charging, inside which R^2 performance (a) is 0.97 and higher.

C. PERFORMANCE OF SOH PREDICTION UNDER NONSTANDARD PRACTICES

1) MINIMUM CHARGING AND DISCHARGING VOLTAGE RANGES REQUIRED FOR ACCURATE SOH PREDICTION

We first determine the minimum voltage ranges between the upper and lower cutoff voltages that are necessary to guarantee accuracy in SOH prediction under nonstandard practices in charging and discharging. For convenience, we represent a minimum voltage range by its center and gap such that the overall ranges can be depicted as a zone in the center-gap space, as shown by the green zones in Figs. 15(b) and 16(b). The green zones in Figs. 15(b) and 16(b) were obtained experimentally based on the CS2 family of the CALCE dataset by selecting the center voltage in-between the upper and lower cutoff voltages with 0.1V resolution and assigning the voltage gap of 0.3V, 0.5V, and 0.7V to each center voltage selected. Then, we obtained SOH prediction corresponding to each center-gap combination and assessed R^2 scores of the predicted SOH, as shown in Figs 15(a) and 16(a) for discharging and charging, respectively. The required minimum voltage ranges, represented as the green zones in Figs 15(b) and 16(b) for discharging and charging, respectively, were then obtained as those combinations that have R^2 scores higher than 0.97. Notice from comparing the green zones of Figs. 15 (b) and 16 (b) that the minimum voltage ranges needed for charging are more stringent than those needed for discharging.

2) PERFORMANCE OF EQUIVALENCE TRANSFORMATION

In Section IV-B, we proposed the equivalence transformation of nonstandard input indices, $(V_1, V_2, Q, VE)^n$, to standard input indices, $(Q, VE)^s$, such that the LSTM stack-based SOH prediction deals only with $(Q, VE)^s$ for the input sequence to reduce a possible combinatorial explosion due to the mixture of standard and nonstandard input indices. We implemented a regression network for the proposed equivalence transformation (refer to Fig. 9) and assessed its performance based on the two datasets obtained from the CS-2 family (Type1 and Type2) of the CALCE dataset for training and testing. The first dataset, EQ1, is generated by using the gap sizes of 0.7, 0.5, and 0.3V with the center voltages fixed at 4.05, 3.85, 3.65, and 3.45V. The second dataset, EQ2, is produced by using the same gap sizes as above, but with the center voltages chosen to meet the minimum voltage range requirement, i.e., (3.5-4.2), (3.7-4.2), (3.6-4.1) and (3.8-4.1)V for charging and (3.5-4.2), (3.7-4.2), (3.6-4.1), (3.4-4.1), (3.2-3.9), (3.4-3.9) and (3.6-3.9)V for discharging. The resulting %RMSE performance of the proposed equivalence transformation is summarized in Table 6. In general, we discovered that the wider the voltage range under nonstandard practices, the better the %RMSE performance of the equivalence transformation becomes for both charging and discharging, if the voltage range covers the required minimum voltage range. Notice a tendency of a reduced %RMSE according to a larger gap size as indicated by the EQ1 result in Table 6. When the gap size is shrunk to 0.3V, the portion of EQ1 data that violates the minimum voltage range requirement increases for charging (refer to Fig. 16(b)), resulting in a rapid increase in %RMSE of Q for charging. On the other hand, the EQ2 result demonstrates that, if the nonstandard voltage range covers the needed minimum voltage range, we can achieve a %RMSE of less than 2% and 8% in the equivalence transformation of VE and Q, respectively, for both charging and discharging.

TABLE 6. Performance of the regression network for equivalence transformation.

Data	Training	Testing	Charging (% RMSE)		Discharging (% RMSE)		
			VE	Q	VE	Q	
EQ1 Center at 4.05, 3.85, 3.65 3.45V	Gap 0.7V	CS2-8 + CS2-35	CS2-21	0.7311	1.9925	1.1185	3.4574
			CS2-36	0.7411	1.4722	1.5151	4.7609
	Gap 0.5V	CS2-8 + CS2-35	CS2-21	1.3038	9.4675	1.1410	2.5528
			CS2-36	1.1237	6.3424	1.5220	5.5005
	Gap 0.3V	CS2-8 + CS2-35	CS2-21	1.7756	26.3124	1.4221	5.9942
			CS2-36	1.4338	20.3368	2.0376	7.9546
EQ2 The same Gap Size with Center chosen for Min. Voltage Range	CS2-8 + CS2-35	CS2-21	1.3880	7.2672	2.1382	8.2240	
		CS2-36	1.1391	7.0139	1.7358	6.8565	
	Type1 + Type2 (60%)	Type1 (40%)	1.0383	6.8584	1.7810	5.7469	
		Type2 (40%)	1.1777	7.0776	1.6238	6.0701	

3) PERFORMANCE OF SOH PREDICTION UNDER NONSTANDARD PRACTICES

Here, SOH prediction under nonstandard practices based on the proposed equivalence transformation is assessed.

TABLE 7. Worst-case performance of SOH prediction under nonstandard practices with equivalence transformation.

Training (Standard)		Testing (Nonstandard)		Charging		Discharging	
Data	Training	Data	Testing	RMSE	R^2	RMSE	R^2
CALCE CS2 (Type1 + Type2)	CS2-8 + CS2-35	EQ1 (Gap 0.7V)	CS2-21+ CS2-36	0.0470 (+0.0113)	0.9664 (-0.0102)	0.0409 (+0.0236)	0.9734 (-0.0219)
		EQ1 (Gap 0.5V)	CS2-21+ CS2-36	0.0627 (+0.0271)	0.9457 (-0.0308)	0.0302 (+0.0130)	0.9834 (-0.0120)
		EQ1 (Gap 0.3V)	CS2-21+ CS2-36	0.0932 (+0.0576)	0.8620 (-0.1146)	0.0411 (+0.0239)	0.9719 (-0.0235)
		EQ2 (Varying Center)	CS2-21+ CS2-36	0.0548 (+0.0192)	0.9573 (-0.0192)	0.0411 (+0.0239)	0.9734 (-0.0220)
	Type1 + Type2 (60%)	EQ2 (Varying Center)	Type1 + Type2 (40%)	0.0325 (+0.0131)	0.8968 (-0.0946)	0.0292 (+0.0126)	0.9299 (-0.0644)

(+/-): the amount of performance degradation from the standard practice

To this end, the proposed equivalence transformation was applied to the EQ1 and EQ2 testing datasets gathered for nonstandard practices to evaluate the performance of the LSTM stack trained for SOH prediction under standard practices. The testing was done based on two scenarios. The first scenario, SC1, tested the worst cases in which all the 20 inputs forming an input sequence are subject to nonstandard practices. Whereas, the second scenario, SC2, tested the cases in which the 20 inputs are configured by a mixture of standard and nonstandard practices. The nonstandard inputs were selected randomly from the EQ1 and EQ2 testing datasets. Table 7 displays the results from SC1 while the numbers in parentheses show how much the performance deviates from the benchmark (refer to Table 3). Overall, the RMSE and R^2 scores in the worst-case scenario are, on average, 0.0364 and 0.9664, respectively, for discharging and 0.0580 and 0.9256, respectively, for charging. This represents the average degradations from standard practices by 0.0224 and 0.0265 in RMSE and R^2 , respectively, for discharging, and 0.0366 and 0.0596 in RMSE and R^2 , respectively, for charging, which validates the effectiveness of equivalence transformation for SOH prediction. Note that, because of the rapid increase in %RMSE of Q, the EQ1 testing with the 0.3V gap shows the largest degradation in SOH prediction for charging. Table 8 shows the result from SC2, where testing is performed by mixing standard and non-standard practices with the ratios of 50%-50% and 30%-70%. In this case, the RMSE and R^2 scores are, on average, 0.0299 and 0.9863, respectively, for discharging and 0.0491 and 0.9641, respectively, for charging.

The overall trend in RMSE and R^2 scores of the proposed SOH prediction according to the ratio of standard and non-standard practices involved in the input sequence is depicted in Fig. 17. As shown, the higher the ratio of standard practices, the higher the accuracy of the predicted SOH

TABLE 8. Performance of SOH prediction under a mixture of non-standard and standard practices.

Training (Standard)		Testing (Mixture)		Charging		Discharging	
Data	Train	Input	Testing	RMSE	R ²	RMSE	R ²
CALCE CS2 (Type1 + Type2)	CS2-8 + CS2-35	Non-S (50%) + Stand (50%)	CS2-21	0.0696 (+0.0090)	0.9486 (-0.0071)	0.0433 (+0.0167)	0.9794 (-0.0127)
			CS2-36	0.0315 (+0.0208)	0.9767 (-0.0207)	0.0218 (+0.0140)	0.9885 (-0.0100)
		Non-S (30%) + Stand (70%)	CS2-21	0.0658 (+0.0052)	0.9519 (-0.0037)	0.0365 (+0.0099)	0.9859 (-0.0062)
			CS2-36	0.0297 (+0.0190)	0.9792 (-0.0182)	0.0206 (+0.0098)	0.9913 (-0.0072)

becomes. Also take note that, for both SC1 and SC2, the performance of discharging-based prediction is marginally superior to charging-based prediction.

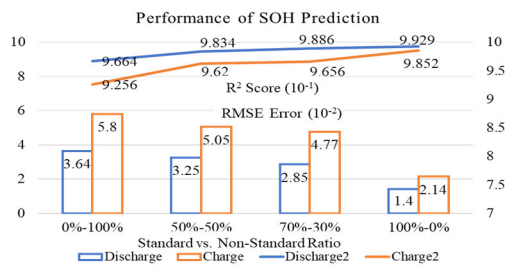


FIGURE 17. RMSE and R² trends according to the standard vs. non-standard ratio of inputs in the input sequence.

4) DISCUSSION

A critical necessity to consider realistic operational conditions in battery SOH prediction, exists, in particular, for application to electric vehicles. Battery SOH prediction can be either charging-based or discharging-based. Charging-based SOH prediction can take advantage of constant charging current that leaves no need for an explicit account of dynamic load conditions. Although an explicit account of dynamic load conditions is necessary, discharging-based SOH prediction can provide more accurate SOH prediction, as verified also in this study (refer to Section VII-B). You et al. [35] utilized a snap-shot voltage(V) and current(I) sequence during charging to input to LSTM for SOH prediction, obtaining about a 2.5% error. Notably, Shu et al. [36] proposed a method for handling nonstandard charging practices by projecting a full charging curve from short-term charging data, with an approximate 2% error. On the other hand, approaches to discharging-based SOH prediction investigate a set of suitable input features that provides a strong correlation with SOH under dynamic load conditions. For instance, Ezemobi et al. [37] proposed ΔV , SOC, ΔS OC, SOE (State of Energy), and ΔSOE ; Venugopal and Vigneswaran [38] proposed to mean of V, I, and temperature, prior SOH, total discharge time and level-wise durations of load current; and Tian and Qin [39] proposed discharge time,

voltage variance and upward voltage after discharge, as input features for deep networks to obtain about 4%, 2.5%, and 1% errors, respectively. The SOH prediction proposed in this study demonstrates its capability of providing state-of-the-art performance even under the presence of more severe yet more realistic operational conditions than before, including a wider variety of nonstandard charging and discharging practices as well as dynamic load conditions. In particular, the novel notions introduced here as the required minimum voltage ranges and the equivalence transformation of nonstandard to standard inputs, together with Q, VE, I_m and SD as input indices, help achieve the efficacy of the proposed SOH prediction under more comprehensive realistic operational conditions.

D. PERFORMANCE OF ONLINE REAL-TIME ANOMALY DETECTION

For assessment of the proposed anomaly detection, we emulated anomalies by using a 3.25AH lithium-ion INR-18650 battery (refer to Table 2 for its specifications). The following two types of anomalies were produced online and in real-time: 1) abrupt alteration of model parameters, $k^p(t)$ and $d^p(t)$, and 2) abnormal alteration of internal resistance and temperature with shunt resistors attached between battery poles.

1) ANOMALY DETECTION THRESHOLD

For the anomaly hypothesis test described in Section VI, we need to set the anomaly threshold, q_α , since the decision on an anomaly is based on $q^p(k) \geq q_\alpha \sim \chi^2(3)$ (refer to Section VI). Note that the anomaly decision is based on well-defined χ^2 statistics between q_α and the confidence probability, $1-\alpha$, with α indicating the significance level. We set α as 0.05 for a 95% of confidence probability, resulting in 7.185 for q_α with 3 DOF of $q^p(k)$ (refer to Table 9).

TABLE 9. Chi-square confidence probability table in terms of significance level, α , and degree of freedom (DOF).

DOF	Significance Level α								
	0.30	0.25	0.20	0.10	0.05	0.025	0.02	0.01	0.005
2	2.108	2.773	3.219	4.605	5.991	7.378	7.824	9.210	10.597
3	3.665	4.108	4.642	6.251	7.815	9.348	9.837	11.345	12.838
4	4.878	5.385	5.989	7.779	9.488	11.143	11.668	13.277	14.860

2) REAL-TIME UPDATE OF REFERENCE MODEL PARAMETERS AND THEIR UNCERTAINTIES

At the start of the p^{th} cycle, the battery model is updated in such a way as to offer the reference for a normal battery aging behavior. As shown in Section V, $(k^p(t), \Delta k^p(t))$, $(d^p(t), \Delta d^p(t))$ and $(R_t^p, \Delta R_t^p)$ are estimated based on the predicted SOH^p and ΔSOH^p while $(R_t, \Delta R_t^p)$, $(C_{cs}, \Delta C_{cs}^p)$ and $(C_{cb}, \Delta C_{cb}^p)$ are updated based on their cyclic degradation rates (refer to Table 1). To this end, we obtained

the initial SOC-OCV curve, $OCV^0(t)$, of the INR-18650 battery by undertaking the initial discharging and charging cycle by applying the same current of 0.68A, as discussed in Section V-B. Furthermore, based on the life cycle charging and discharging experiment, we obtained the functional relationship between SOH^p and $R_i^p, R_t^p = -0.0357 \times SOH^p + 0.17$.

TABLE 10. Battery SOH and model parameters with their uncertainties bounds updated at the 100th cycle.

Parameter	SOH^{100}	R_i^{100}	C_{cb}^{100}	C_{cs}^{100}	R_t^{100}
Update	0.964	0.136	12,128.6	89.2	0.07
Uncertainty	ΔSOH^{100}	ΔR_i^{100}	ΔC_{cb}^{100}	ΔC_{cs}^{100}	ΔR_t^{100}
	0.023	0.0008	69.1	0.51	0.025

TABLE 11. Battery SOH and model parameters with their uncertainties bounds updated at the 200th cycle.

Parameter	SOH^{200}	R_i^{200}	C_{cb}^{200}	C_{cs}^{200}	R_t^{200}
Update	0.94	0.136	12,017.2	88.4	0.09
Uncertainty	ΔSOH^{200}	ΔR_i^{200}	ΔC_{cb}^{200}	ΔC_{cs}^{200}	ΔR_t^{200}
	0.034	0.001	271.6	2.0	0.05

Tables 10 and 11 depict the predicted SOHs and their uncertainties as well as the updated model parameters and their uncertainties at the respective 100th and 200th cycles selected for the anomaly test. Note that $(k^p(t), \Delta k^p(t))$ and $(d^p(t), \Delta d^p(t))$ were obtained by the SOC-OCV curves at the p^{th} cycle derived from $OCV^0(t)$ and SOH^p (refer to Section V-B). The green and red curves in Fig. 18 (a), (c), and (e) illustrate, respectively, $k^{200}(t)$ and $d^{200}(t)$ generated from $OCV^0(t)$ and SOH^{200} . Finally, the uncertainty bounds associated with the measured terminal current and voltage, $\Delta I^p(t)$ and $\Delta V^p(t)$, were set by the manufacturer-provided sensor uncertainties (0.05%).

3) ANOMALY EXPERIMENT 1: ABRUPTLY ALTERATION OF MODEL PARAMETERS

In Experiment 1, we produced an anomaly by abruptly altering the capacity-related model parameters, $k^{200}(t)$ and $d^{200}(t)$, at the 200th discharging cycle of the INR-18650 battery. Three different modes of the anomaly were emulated to examine how different traits in anomaly affect detection performance. They are: 1) the abrupt mode generated by abruptly changing $k^{200}(t)$ and $d^{200}(t)$ at 5,000 sec. for the duration of 2,500 sec. by adding 1.0 to both parameters (refer to Fig. 18 (a)), 2) the gradual mode generated by adding a linearly increasing bias to $k^{200}(t)$ and $d^{200}(t)$ from 5,000 s. to 10,000 s. (refer to Fig. 18 (c)) and 3) the random mode generated by abruptly changing $k^{200}(t)$ and $d^{200}(t)$ at a randomly chosen time between 5,000 s. and 10,000 s. (refer to Fig. 18 (e)). The result of anomaly detection for the above 3 modes of anomalies is illustrated

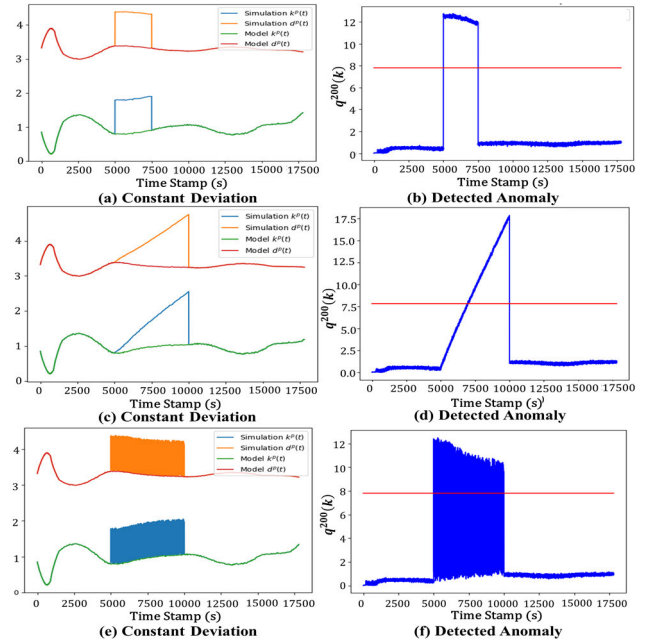


FIGURE 18. 3 modes of anomaly detection experiments: (a), (b): abrupt mode, (c), (d): gradual mode, and (e), (f): random mode. The red crosslines in (b), (d), and (f) are the anomaly detection threshold, q_{α} , with 95% confidence.

in Figs. 18 (b), (d), and (f), where the anomaly threshold, q_{α} , corresponding to 95% confidence in the decision is indicated by the red crosslines. Figs. 18 (b), (d), and (f) indicate that the proposed anomaly detection based on the uncertainty-weighted distance, $q^p(k)$, gives high accuracy and sensitivity in detecting different modes of anomalies. Fig. 18 (d) indicates that a gradual increase in the level of anomaly is directly reflected in a gradual increase in $q^p(k)$. This implies that $q^p(k)$ can serve as an anomaly indicator effective for identifying a slow mode of an anomaly with the capability of exposing the level of anomaly. Moreover, Figs. 18 (b) and (f) show that $q^p(k)$ is not only level-sensitive but also time-sensitive as it indicates an anomaly in synchrony with the time when the anomaly is in place regardless of how abrupt and short the temporal pattern of the anomaly is.

4) ANOMALY EXPERIMENT 2: ABNORMAL ALTERATION OF LOAD CURRENT AND TEMPERATURE WITH SHUNT RESISTORS

In Experiment 2, we generated an anomaly by abruptly switching on and off the shunt resistors connected between two battery poles at the 100th discharging cycle of the INR-18650 battery. Refer to Table 10 for the predicted SOH and updated model parameters at the 100th cycle. Experiment 2 was performed based on two different modes of the anomaly: 1) the abrupt shunt mode in which 5 ohms of shunt resistor are abruptly switched on at 300 s. and off at 600 s. and 2) the gradual shunt mode in which 10 ohms of shunt resistor initially switched on at 600 s. is gradually reduced by 1 ohm

at every 600 s. interval until the resistance reaches 1 ohm before switching off at 6,600 s. With the shunting resistors connecting two battery poles, Experiment 2 simulates an abnormal change in battery internal resistance as well as an abnormal rise in battery temperature to test the proposed anomaly detection method. Figs. 19 (a) and (b) show temporal variations of $q^{100}(k)$ associated with the abrupt shunt and gradual shunt modes of anomalies, respectively. Fig. 19 (a) depicts that, same as Experiment 1, $q^{100}(k)$ accurately indicates an anomaly exactly at the time of switching the shunt resistor on at 300 s. Notice, however, that, unlike Experiment 1, $q^{100}(k)$ indicating the level of anomaly is increased gradually during the time of shunting. This increase of $q^{100}(k)$ is considered due to the temperature rise caused by the battery overload from shunting.

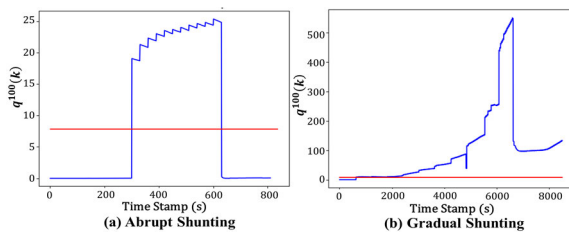


FIGURE 19. $q^{100}(k)$ profiles for the abrupt shunt (a) and the gradual shunt (b) modes of anomalies. The red crosslines represent the anomaly decision threshold, q_{α} , that corresponds to a 95% confidence level in the decision.

On the other hand, Fig. 19 (b) shows the $q^{100}(k)$ profile associated with the gradual shunt mode of anomaly. In Fig. 19 (b), $q^{100}(k)$ is stepped up at the time of switching the shunt resistor on at 600 s. to indicate an anomaly occurrence. Then, $q^{100}(k)$ is kept on increasing its anomaly level according to the increase in the reduction of shunt resistance by 1 ohm/600 s. rate. In particular, we observe that exponential growth and the explosion of $q^{100}(k)$ take place as the shunt resistance is reduced further down below 4 ohms at 4,200 s. This phenomenon of the $q^{100}(k)$ explosion is considered due to battery overheating and thermal runaway caused by the excessive flow of current inside the battery. Fig. 19 (b) shows that, even after the shunt resistor is switched off at 6,600 s., $q^{100}(k)$ is remained higher than q_{α} , indicating the failure of the battery to return to its normal state due to permanent damage inflicted on the battery from overheating. In summary, $q^p(k)$ proves to be an accurate and sensitive anomaly indicator capable of quantifying the level of anomaly or the probability of a battery being in the state of anomaly. Finally, as depicted in Section III, upon detecting an anomaly, we skip filtering a predicted state so that the model keeps identifying the anomaly without adapting its state to the anomaly for robust decision. Note that we may set an optimal threshold for filtering decisions q'_{α} , separately from that for anomaly decision, q_{α} , such that a slow mode of anomalies can subsequently be exposed through the accumulation of their anomaly effects.

5) DISCUSSION

As described in Section I, anomaly detection based on identifying outliers from the cluster of battery normal behaviors is conceptually simple to implement as long as statistically well-represented ground truth data are available for cluster formation. However, clusters formed based on the data collected along a life cycle of battery aging under a wide variety of operational conditions have their distributions wildly dispersed, increasing the ambiguity in anomaly detection, in particular, at an earlier cycle. The fundamental trade-off between accuracy and generality that exists in cluster-based anomaly detection needs to be further addressed. On the other hand, anomaly detection based on the deviation between the predicted and observed states of a battery relies on the accuracy of the model used for the prediction. As noted, batteries have yet to be modeled to accurately represent a life-cycle aging behavior due to complex nonlinear electrochemical battery dynamics [25]. A real-time fitting of model parameters to actual measurements [20], [21], [22], [23], [24] proposed as an alternative way of securing model accuracy may force the model to adapt, in particular, to a slowly varying abnormal behavior. The fundamental trade-off between accuracy and sensitivity that exists in model-based anomaly detection also needs to be further addressed. The proposed approach mitigates such trade-offs by cyclically predicting battery SOHs to follow battery aging while model parameters are temporally updated within a cycle based on the predicted SOHs without adapting to measurements. The integration of two separate processes, the data-driven cyclic prediction of battery aging and the model-based prediction of normal behavior within a cycle with the model updated to battery aging allows the proposed approach to effectively provide accurate, sensitive, and robust anomaly detection along a life cycle of batteries under a wide variety of realistic operational conditions.

VIII. CONCLUSION

In this study, we proposed an approach to online and real-time SOH prediction and anomaly identification for rechargeable batteries during their life cycles, emphasizing real-world operational conditions. Nonstandard charging and discharging practices as well as dynamic load conditions were considered for actual operational conditions. First, to differentiate anomalies from normal aging, we introduced a method for defining a life-cycle reference model by cyclically updating model parameters and their uncertainties based on the predicted SOH and its uncertainty at each cycle. To achieve this, we presented a thorough and reliable method for SOH prediction under dynamic load conditions and unconventional charging and discharging procedures. In particular, we proposed the equivalence transformation as a novel method for addressing a possible combinatorial problem in SOH prediction under non-standard practices while developing the minimum non-standard voltage ranges

required for SOH prediction. We confirmed by experiment that we could achieve the state-of-the-art performance in SOH prediction under the aforementioned realistic operational conditions by combining the proposed equivalence transformation with Q, VE, I_m , and SD selected as the input features to LSTM stack-based SOH prediction. Finally, we demonstrated by experiment that the proposed CPF-based hypothesis test together with the SOH-based model update could provide accurate and sensitive anomaly detection, supported by the anomaly indicator, $q^p(k)$, capable of representing the level of an anomaly for a slow mode of anomaly. In the future, we plan to extend the experiment with more custom-collected datasets to cover a wider variety of real-world battery operational conditions. In the future, we plan to extend the experimental verification with more custom-collected datasets to cover a wider variety of real-world battery operational conditions that affect battery normal aging. In addition, we plan to deepen our investigation on detecting, tracing, and diagnosing a wider variety of real-world anomalies including, in particular, various slow modes of anomalies. Also, we are interested in improving accuracy in modeling the normal aging behavior of a battery by adopting a more comprehensive battery model representing a wider variety of aging factors existing in reality. Notably, we recognize that we need to deal with either the lack of available datasets or the difficulty in collecting a sufficient size of datasets when deep learning-based approaches are involved in either SOH prediction or anomaly detection. Therefore, we are interested in investigating in the future whether or not the application of continual learning frameworks to deep learning-based battery SOH prediction and anomaly detection is feasible.

REFERENCES

- [1] X. Hu, K. Zhang, K. Liu, X. Lin, S. Dey, and S. Onori, "Advanced fault diagnosis for lithium-ion battery systems: A review of fault mechanisms, fault features, and diagnosis procedures," *IEEE Ind. Electron. Mag.*, vol. 14, no. 3, pp. 65–91, Sep. 2020.
- [2] N. Al-Zubaidi R-Smith, M. Leitner, I. Alic, D. Toth, M. Kasper, M. Romio, Y. Surace, M. Jahn, F. Kienberger, A. Ebner, and G. Gramse, "Assessment of lithium ion battery ageing by combined impedance spectroscopy, functional microscopy and finite element modelling," *J. Power Sources*, vol. 512, Nov. 2021, Art. no. 230459.
- [3] K. Bhaskar, A. Kumar, J. Bunce, J. Pressman, N. Burkell, and C. D. Rahn, "Data-driven thermal anomaly detection in large battery packs," *Batteries*, vol. 9, no. 2, p. 70, Jan. 2023.
- [4] C. Pascoal, M. R. de Oliveira, R. Valadas, P. Filzmoser, P. Salvador, and A. Pacheco, "Robust feature selection and robust PCA for internet traffic anomaly detection," in *Proc. IEEE INFOCOM*, Mar. 2012, pp. 1755–1763.
- [5] X. Li, J. Li, A. Abdollahi, and T. Jones, "Data-driven thermal anomaly detection for batteries using unsupervised shape clustering," in *Proc. IEEE 30th Int. Symp. Ind. Electron. (ISIE)*, Jun. 2021, pp. 1–6.
- [6] C. Liu, J. Tan, H. Shi, and X. Wang, "Lithium-ion cell screening with convolutional neural networks based on two-step time-series clustering and hybrid resampling for imbalanced data," *IEEE Access*, vol. 6, pp. 59001–59014, 2018.
- [7] L. Yao, Y. Xiao, X. Gong, J. Hou, and X. Chen, "A novel intelligent method for fault diagnosis of electric vehicle battery system based on wavelet neural network," *J. Power Sources*, vol. 453, Mar. 2020, Art. no. 227870.
- [8] S. N. Haider, Q. Zhao, and X. Li, "Data driven battery anomaly detection based on shape based clustering for the data centers class," *J. Energy Storage*, vol. 29, Jun. 2020, Art. no. 101479.
- [9] C. Sun, Z. He, H. Lin, L. Cai, H. Cai, and M. Gao, "Anomaly detection of power battery pack using gated recurrent units based variational autoencoder," *Appl. Soft Comput.*, vol. 132, Jan. 2023, Art. no. 109903.
- [10] H. Shin, J. Lee, and P. Kim, "Causality-Seq2Seq model for battery anomaly detection," *Int. J. Aeronaut. Space Sci.*, vol. 24, no. 1, pp. 284–293, Feb. 2023.
- [11] S. A. Gadsden and S. R. Habibi, "Model-based fault detection of a battery system in a hybrid electric vehicle," in *Proc. IEEE Vehicle Power Propuls. Conf. (VPPC)*, Sep. 2011, pp. 1–6.
- [12] Z. Liu and H. He, "Sensor fault detection and isolation for a lithium-ion battery pack in electric vehicles using adaptive extended Kalman filter," *Appl. Energy*, vol. 185, pp. 2033–2044, Jan. 2017.
- [13] R. Tunga, C. Murguia, and J. Ruths, "Tuning windowed chi-squared detectors for sensor attacks," in *Proc. Annu. Amer. Control Conf. (ACC)*, Milwaukee, WI, USA, Jun. 2018, pp. 1752–1757.
- [14] Z. Geng, S. Wang, M. J. Lacey, D. Brandell, and T. Thiringer, "Bridging physics-based and equivalent circuit models for lithium-ion batteries," *Electrochimica Acta*, vol. 372, Mar. 2021, Art. no. 137829.
- [15] R. Zhao, J. Liu, and J. Gu, "The effects of electrode thickness on the electrochemical and thermal characteristics of lithium ion battery," *Appl. Energy*, vol. 139, pp. 220–229, Feb. 2015.
- [16] X. Hu, S. Li, and H. Peng, "A comparative study of equivalent circuit models for Li-ion batteries," *J. Power Sources*, vol. 198, pp. 359–367, Jan. 2012.
- [17] Y. Che, J. Jia, Y. Yang, S. Wang, and W. He, "Parameter identification of 3R-C equivalent circuit model based on full life cycle database," *J. Elect. Eng. Technol.*, vol. 13, no. 4, pp. 1759–1768, 2018.
- [18] D. Pola, F. Guajardo, E. Jofre, V. Quintero, A. Perez, D. Acuna, and M. Orchard, "Particle-filtering-based state-of-health estimation and end-of-life prognosis for lithium-ion batteries at operation temperature," in *Proc. Annu. Conf. Prognostics Health Manage. Soc. (PHM)*, 2016, pp. 1–10.
- [19] Y. Wang, J. Tian, Z. Sun, L. Wang, R. Xu, M. Li, and Z. Chen, "A comprehensive review of battery modeling and state estimation approaches for advanced battery management systems," *Renew. Sustain. Energy Rev.*, vol. 131, Oct. 2020, Art. no. 110015.
- [20] B. Xia, Z. Lao, R. Zhang, Y. Tian, G. Chen, Z. Sun, W. Wang, W. Sun, Y. Lai, M. Wang, and H. Wang, "Online parameter identification and state of charge estimation of lithium-ion batteries based on forgetting factor recursive least squares and nonlinear Kalman filter," *Energies*, vol. 11, no. 1, p. 3, Dec. 2017.
- [21] H. He, R. Xiong, and H. Guo, "Online estimation of model parameters and state-of-charge of LiFePO₄ batteries in electric vehicles," *Appl. Energy*, vol. 89, no. 1, pp. 413–420, Jan. 2012.
- [22] V. Sangwan, A. Sharma, R. Kumar, and A. K. Rathore, "Equivalent circuit model parameters estimation of Li-ion battery: C-rate, SOC and temperature effects," in *Proc. IEEE Int. Conf. Power Electron., Drives Energy Syst. (PEDES)*, Dec. 2016, pp. 1–6.
- [23] F. Feng, R. Lu, G. Wei, and C. Zhu, "Online estimation of model parameters and state of charge of LiFePO₄ batteries using a novel open-circuit voltage at various ambient temperatures," *Energies*, vol. 8, no. 4, pp. 2950–2976, Apr. 2015, doi: 10.3390/EN8042950.
- [24] M. Sitterly, L. Y. Wang, G. G. Yin, and C. Wang, "Enhanced identification of battery models for real-time battery management," *IEEE Trans. Sustain. Energy*, vol. 2, no. 3, pp. 300–308, Jul. 2011.
- [25] H. Tian, P. Qin, K. Li, and Z. Zhao, "A review of the state of health for lithium-ion batteries: Research status and suggestions," *J. Cleaner Prod.*, vol. 261, Jul. 2020, Art. no. 120813.
- [26] M. A. Bakr and S. Lee, "A general framework for data fusion and outlier removal in distributed sensor networks," in *Proc. IEEE Int. Conf. Multisensor Fusion Integr. Intell. Syst. (MFI)*, Nov. 2017, pp. 91–96.
- [27] M. A. Bakr and S. Lee, "A framework of covariance projection on constraint manifold for data fusion," *Sensors*, vol. 18, no. 5, p. 1610, May 2018.
- [28] M. Pecht. (2017). *Battery Data Set. CALCE*. CALCE Battery Research Group. [Online]. Available: <https://web.calce.umd.edu/batteries/index.html>

- [29] R. Walpole, R. Myers, S. Myers, and K. Ye, *Probability and Statistics for Engineers and Scientists*. Basingstoke, U.K.: Macmillan, 1993.
- [30] A. Kim and S. Lee, "Online state of health estimation of batteries under varying discharging current based on a long short term memory," in *Proc. 15th Int. Conf. Ubiquitous Inf. Manage. Commun. (IMCOM)*, Jan. 2021, pp. 1–6.
- [31] A. Kim and S. Lee, "Online battery SOH prediction under intra-cycle variation of discharge current and non-standard charging and discharging practices," in *Proc. Annu. Conf. PHM Soc.*, 2022, vol. 14, no. 1, pp. 1–11.
- [32] S. Hochreiter and J. Schmidhuber, "Long short-term memory," *Neural Comput.*, vol. 9, no. 8, pp. 1735–1780, Nov. 1997.
- [33] N. Williard, W. He, and M. Pecht, "Model based battery management system for condition based maintenance," in *Proc. Prognostics Health Manag. Solutions Conf.*, Dayton, OH, USA, Apr. 2012, pp. 24–26.
- [34] F. Leng, C. M. Tan, and M. Pecht, "Effect of temperature on the aging rate of Li ion battery operating above room temperature," *Sci. Rep.*, vol. 5, no. 1, Aug. 2015, Art. no. 12967, doi: [10.1038/SREP12967](https://doi.org/10.1038/SREP12967).
- [35] G.-W. You, S. Park, and D. Oh, "Diagnosis of electric vehicle batteries using recurrent neural networks," *IEEE Trans. Ind. Electron.*, vol. 64, no. 6, pp. 4885–4893, Jun. 2017.
- [36] X. Shu, G. Li, Y. Zhang, J. Shen, Z. Chen, and Y. Liu, "Online diagnosis of state of health for lithium-ion batteries based on short-term charging profiles," *J. Power Sources*, vol. 471, Sep. 2020, Art. no. 228478.
- [37] E. Ezemobi, M. Silvagni, A. Mozaffari, A. Tonoli, and A. Khajepour, "State of health estimation of lithium-ion batteries in electric vehicles under dynamic load conditions," *Energies*, vol. 15, no. 3, p. 1234, Feb. 2022, doi: [10.3390/EN15031234](https://doi.org/10.3390/EN15031234).
- [38] P. Venugopal and T. Vigneswaran, "State-of-health estimation of Li-ion batteries in electric vehicle using IndRNN under variable load condition," *Energies*, vol. 12, no. 22, p. 4338, Nov. 2019, doi: [10.3390/EN12224338](https://doi.org/10.3390/EN12224338).
- [39] H. Tian and P. Qin, "State of health prediction for lithium-ion batteries with a novel online sequential extreme learning machine method," *Int. J. Energy Res.*, vol. 45, no. 2, pp. 2383–2397, Feb. 2021.



SUKHAN LEE (Life Fellow, IEEE) received the B.S. and M.S. degrees in electrical engineering from Seoul National University, South Korea, in 1972 and 1974, respectively, and the Ph.D. degree in electrical engineering from Purdue University, West Lafayette, IN, USA, in 1982. From 1983 to 1997, he was with the Department of Electrical Engineering and Computer Science, University of Southern California. From 1990 to 1997, he was with the Jet Propulsion Laboratory, California Institute of Technology. From 1998 to 2003, he was the Executive Vice President and the Chief Research Officer with the Samsung Advanced Institute of Technology. Since 2003, he has been a Professor of information and communication engineering with Sungkyunkwan University. His research interests include cognitive robotics, intelligent systems, deep learning, and micro/nano electro-mechanical systems. He is currently a Life Fellow of the Korea National Academy of Science and Technology



AREUM KIM received the B.S. degree in electronic and electrical engineering from Chung-Ang University, in 2015. She is currently pursuing the master's degree with Sungkyunkwan University. From 2016 to 2019, she was an Engineer with HUMAX. Her research interests include PHM based on intelligent systems and time series analysis with machine learning.

...